Mechanical properties of microconstituents in Nb-Si-Ti alloy by micropillar compression and nanoindentation

Enyu Guo, Sudhanshu S. Singh, Chandrashekara S. Kaira, Xianyu Meng, Yanjin Xu, Liangshun Luo, Mingyue Wang, Nikhilesh Chawla

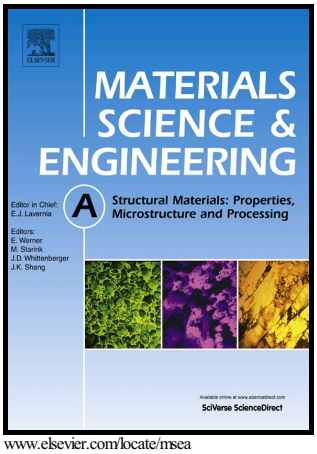

www.elsevier.com/locate/msea

PII: S0921-5093(17)30077-1
DOI: http://dx.doi.org/10.1016/j.msea.2017.01.058
Reference: MSA34620

To appear in: *Materials Science & Engineering A*

Received date: 14 September 2016
Revised date: 17 January 2017
Accepted date: 19 January 2017

Cite this article as: Enyu Guo, Sudhanshu S. Singh, Chandrashekara S. Kaira Xianyu Meng, Yanjin Xu, Liangshun Luo, Mingyue Wang and Nikhilesh Chawla, Mechanical properties of microconstituents in Nb-Si-Ti alloy by micropillar compression and nanoindentation, *Materials Science & Engineering A,* http://dx.doi.org/10.1016/j.msea.2017.01.058

Mechanical properties of microconstituents in Nb-Si-Ti alloy by micropillar compression and nanoindentation

Enyu Guo[1], Sudhanshu S.Singh[1,5], Chandrashekara S. Kaira[1], Xianyu Meng[2], Yanjin Xu[4], Liangshun Luo[2], Mingyue Wang[3*], Nikhilesh Chawla[1**]

[1]Materials Science and Engineering, Arizona State University, Tempe, AZ 85287-6106, USA
[2]School of Materials Science and Engineering, Harbin Institute of Technology, Harbin, Heilongjiang 150001, P. R. China
[3]International Research Institute for Multidisciplinary Science, Beihang University, Beijing 100191, P. R. China
[4]AVIC Beijing Aeronautical Manufacturing Technology Research Institute, Beijing 100024, P. R. China
[5]Department of Materials Science and Engineering, Indian Institute of Technology Kanpur, Uttar Pradesh 208016, India

wangmy07@mails.thu.edu.cn (Mingyue Wang)

nchawla@asu.edu_（Nikhilesh Chawla)

*Authors to whom all correspondence should be addressed,

Abstract

The micromechanical properties of both Nb solid solution (Nbss) and $(Nb,Ti)_3Si$ silicide in a ternary Nb-16Si-22Ti (in at.%) alloy were evaluated by nanoindentation and micropillar compression techniques. Nanoindentation tests showed that $(Nb,Ti)_3Si$ possesses much higher hardness (15.6 ± 0.6 GPa) and Young's modulus (253.3 ± 8.4 GPa) than Nbss (5.2 ± 0.4 GPa and 124.9 ± 5.1 GPa, respectively).

Stress-strain curves of each constituent were obtained by micropillar compression. The stress-strain behavior showed that $(Nb,Ti)_3Si$ exhibited a brittle fracture mode, while Nbss was able to bear large ductile deformation. The compressive failure strength of $(Nb,Ti)_3Si$ intermetallic and yield strength of Nbss were found to be 8.4 ± 1.2 GPa and 0.9 ± 0.1 GPa, respectively. The fracture toughness of the $(Nb,Ti)_3Si$ phase evaluated by cracks emanating from nanoindentation, was measured to be ~2.3 MPa-$m^{1/2}$.

Keywords: Intermetallics; Mechanical properties; High temperature alloy; Fracture toughness; Micropillar compression

1. Introduction

Nb-Si based alloys have gained attention as important advanced structural materials for ultra-high temperature applications in aerospace due to their excellent oxidation resistance at high temperature, high melting points (>1750 ^{o}C), high mechanical strength, and environmental stability [1-4]. The excellent mechanical properties of Nb-Si alloys are due to their multiphase microstructure containing Nb solid solution (Nbss) and stiff intermetallic silicides (Nb_5Si_3 or Nb_3Si). The bulk deformation behavior of these materials is greatly determined by many factors, such as the volume fraction, grain size and morphologies of each constituent. Therefore, a lot of work have been performed to optimize the mechanical properties of the Nb-Si based alloys by optimizing processing [5-7] and alloy compositions [4, 8-11]. Among the Nb-Si based alloys, Nb-Si-Ti forms an important multiple component alloy. Studies have shown that the addition of Ti in the Nb-Si system plays a key role in improving the fracture toughness and ductility of the Nb solid solution, as well as their oxidation resistance [1, 6, 11-13]. In addition, Ti was reported to stabilize the Nb_3Si phase and, thus, to form a Nbss\Nb_3Si microstructure [14]. It is well recognized that the mechanical properties of multi-phase materials are greatly dependent on the intrinsic properties of each microconstituent. Therefore, understanding of mechanical behavior of each microconstituent in the alloy is of great importance.

Nanoindentaion is a very useful technique to obtain the micromechanical properties of individual microconstituent. It has been successfully used to understand

the mechanical behaviour of intermetallic phases [7, 9, 15], including silicides in Nb-Si based alloys [7, 9]. Using the load-displacement curves, hardness and Young's modulus values can be extracted. In addition, other mechanical properties, such as fracture toughness, can also be obtained [16]. The limitation of this technique is that the flow of the material is constrained from the surrounding region during indentation deformation and the overall stress state is not homogeneous. Thus, it is very difficult to evaluate the uniaxial stress-strain behavior from sharp tip indentation. Recently, micropillar compression has merged as an alternative technique, where there is no constraint from the surrounding material and therefor near uniaxial stress-strain behaviour can be obtained. This technique has already been used in a wide range of materials [17-21], including refractory metals such as Nb [22, 23]. However, to the best of our knowledge, micropillar compression studies of the Nb-Si alloys have not yet been performed.

In this work, we have utilized nanoindentation and micropillar compression to understand and compare the different mechanical deformation behavior of Nb solid solution (Nbss) and the silicide phase ($(Nb, Ti)_3Si$) in a ternary Nb-Si-Ti alloy. Critical mechanical properties, such as hardness, Young's modulus, and fracture toughness were obtained from the nanoindentation tests and the uniaxial deformation behaviour of each individual constituent was obtained by the micropillar compression technique.

2. Material and experimental procedure

Samples with nominal compositions of Nb-16Si-22Ti (all in at.%) were prepared

by arc melting Nb (99.9%), Si (99.99%) and Ti (99.9%). The alloy was remelted four times under purified Ar gas, for homogenous distribution of the alloying elements. The material was then cast in a water cooled copper mold to obtain the cast ingot. Small samples ($8\times8\times3$ mm^3) were machined from the central region of the cast ingot, where equiaxed grains were most likely to be found. Samples were initially ground and then polished to a 1 μm diamond finish. Final polishing was performed with 0.05 μm colloidal silica to obtain a smooth surface on the sample. X-ray diffraction (XRD) (D/max-RB, Rigaku Co., Tokyo, Japan) was performed to determine the phases present in the alloy. The scan used a step size of 0.02^o for a range of $20\text{-}100^o$ with x-rays using CuKα radiation (0.15418 Å).

Micropillars were fabricated with a dual-beam focused ion beam (FIB) in a scanning electron microscope (SEM) (Nova 200 NanoLab FEGSEM/ FIB, FEI Co, Oregon, U.S). Before fabrication of the micropillars, energy dispersive spectroscopy (EDS) analysis was performed to identify the phases. Micropillars of very similar dimensions were fabricated in both intermetallic ($(Nb,Ti)_3Si$) and Nbss phases. Initially, a beam of Ga+ ions accelerated at 30 keV with a current of 20 nA was used to mill out a circular trench ~25 μm in diameter with a coarse pillar of 10 μm diameter at the center. Then, the current was gradually decreased from 1 to 0.1 nA to obtain micropillars with a final nominal top diameter of approximately 2 μm. By this milling approach pillars having a typical aspect ratio (length/diameter) of 3-3.5 and a taper of less than 3^o were obtained. The intermediate value of aspect ratio used in this study minimized the buckling and bending issues during compression of samples

having lower and higher aspect ratio, respectively. After fabrication of the pillars, EDS was again performed at the base of the pillar to check the compositions.

Nanoindentation experiments were conducted on a commercial nanoindenter XP system (Keysight Technologies, Santa Clara, CA) equipped with an optical microscope for imaging. The indenter tip was calibrated with a fused silica sample. Continuous stiffness measurement (CSM) technique was used to measure the hardness and Young's modulus with respect to indentation depth. The samples were allowed to thermally equilibrate until the drift rate was measured to be below 0.05 nm s^{-1}. Tests on both phases were conducted at a strain rate of around 0.05/s. Tests were conducted to a maximum indention depth of 1000 nm. Tests on the $(Nb,Ti)_3Si$ silicide were conducted to a maximum depth of 500 nm. At least 15 indentations were performed on each phase. After testing, deformation around the indentations was examined using a scanning electron microscope (XL30 Environmental FEG, FEI Co, Oregon). For the micropillar compression testing, the micropillars were compressed with a Berkovich (three-sided pyramid) diamond indenter tip having a flat triangular cross-section (10 µm side). The tests were carried out at a prescribed displacement rate of 5 nm/s, corresponding to an initial strain rate of ~10^{-3} s^{-1}. The actual displacement due to the compliance of the indenter tip and the substrate matrix was corrected using the Sneddon's correction criterion [24].

3. Results and discussion

3.1 Microstructure and phase identification

Typical back-scattered electron (BSE) images of the as-cast sample are shown in Fig. 1. Combined analysis of BSE images, x-ray diffraction (Fig. 1c), and energy dispersive spectroscopy (EDS) (Table 1), show that the microstructure was comprised of white islands of Nb solid solution (Nbss), light gray silicide $(Nb,Ti)_3Si$, and a small amount of fine dark phases distributed between Nbss and $(Nb,Ti)_3Si$ phases. EDS analysis indicated that most of the dark phases were eutectic $(Nb,Ti)_5Si_3$ within the eutectic microstructure region of $(Nb,Ti)_5Si_3$ and Nbss. A very small amount of complex Ti segregated phase was also observed at Nbss phase boundaries, as shown in Fig. 1b. Eutectic $(Nb,Ti)_5Si_3$ microconstituent was not identified in the X-ray pattern due to its relatively low phase fraction. It can be seen that the distribution of Ti in the alloy is not uniform. It was observed mainly in the eutectic $(Nb,Ti)_5Si_3$ (30.4 at.%) and $(Nb,Ti)_3Si$ silicide (22.5 at.%) compared to the Nbss phase (17.2 at.%). Nb is mainly concentrated in the Nbss phase. The addition of Ti has been found to stabilize the $(Nb,Ti)_3Si$ phase [14, 25] and, thus, help to form a Nbss\$(Nb,Ti)_3Si$ microstructure, as found in this study. It is known that the decomposition of $(Nb,Ti)_3Si$ phase is a very slow process. Therefore, the formation of $(Nb,Ti)_5Si_3$ phase can be attributed to rapid solidification in the water cooled copper crucible. This can be further verified by the fact that $(Nb,Ti)_5Si_3$ phases were found at the phase boundaries, suggesting that this phase was caused by compositional undercooling by Ti addition, rather than the product of rapid decomposition of the $(Nb,Ti)_3Si$ phase. It is expected that Ti will be rejected into the liquid phase during the solidification process, leading to the segregation of Ti in front of the solid- liquid interface. One can

see that the addition of Ti plays an important role on the $(Nb,Ti)_5Si_3$ phase formation. Similar observations of microstructure formation in Nb-Si-Ti alloys have also been reported [26, 27].

3.2 Nanoindentation and fracture toughness

Fig. 2 shows typical results of the nanoindentation experiments on the Nbss and $(Nb,Ti)_3Si$ phases. The load at the peak indentation displacement of 1000 nm is higher (222 mN) for the $(Nb,Ti)_3Si$ phase than the Nbss phase (101 mN), indicating that the intermetallic $(Nb,Ti)_3Si$ phase is much harder than the Nbss phase.

When the continuous stiffness measurement (CSM) method is used, the modulus and hardness are measured over "plateau values" of displacement, i.e., a range of displacement where the modulus and hardness are not changing significantly. In our experiments, the values of Young's modulus (E) and hardness (H) for a given indentation were taken as the average value over 75–150 nm and 100–200 nm for the $(Nb,Ti)_3Si$ and Nbss, respectively, as indicated in the Fig. 2b and 2c. It can be seen that both the Young's modulus (Fig. 2b) and hardness (Fig. 2c) of $(Nb,Ti)_3Si$ phase is significantly higher than those of the Nbss phase. The values show that the average hardness and Young's modulus for the $(Nb,Ti)_3Si$ phase are higher than the Nbss phase by about 200% and 80%, respectively. The higher hardness of $(Nb,Ti)_3Si$ phase (tP32) than the Nbss phase (bcc) can be attributed to its complex crystal structure with low symmetry, absence of closed packed planes, and less active slip system.

The deformation around the indentations made on these two different phases exhibited totally different deformation behavior, as shown in Fig. 3. In the case of $(Nb,Ti)_3Si$ phase, indentation-induced cracks at the corners of the indentation are visible (these likely took place at much higher indentation depths than the displacements used to measure modulus and hardness), suggesting a brittle characteristic of the silicide $(Nb,Ti)_3Si$ phase. The corner cracks were observed in both 500 nm and 1000 nm depth of indentation, as shown in Fig. 3b and 3d, respectively. On the contrary, no cracks were observed around the indentations made on Nbss phase. Instead, pile-up was observed around the indentations indicating a significant amount of plastic deformation (Fig. 3a). This is further confirmed by the observation of the indentations made on both $(Nb,Ti)_3Si$ and Nbss phases (Fig. 3c). Pile-up is observed in Nbss, but a crack is formed on $(Nb,Ti)_3Si$ phase. Due to very small size of $(Nb,Ti)_5Si_3$ phase (~2-3 μm), micromechanical analysis on this phase was very difficult. Therefore, evaluation of mechanical properties of this phase was not performed in this study.

The measurement of the fracture toughness (K_c) of brittle phases is important to understand the mechanical performance of the bulk material. The fracture toughness value can be evaluated through indentation experiments by measuring the cracks at the corners of the indentation. Depending on the indenter geometry and crack morphology, several expressions have been proposed to determine the K_c using indentation. The most widely used models include expressions for radial cracks proposed by Anstis *et al*. [28], expressions for the Palmqvist crack proposed by

Niihara *et a.l* [29], also further modified by Laugier [30]. The expressions proposed by Anstis *et al*, Niihara *et al*, and Laugier can be written in the forms of Eq. (1), (2) and (3), respectively.

$$K_c = A \times (E/H)^n \times (P/c^{3/2}) \quad (1)$$

$$K_c = \phi \times (E/0.927H)^{2/5} \times (P/a\sqrt{l}) \quad (2)$$

$$K_c = x_v \times (a/l)^{1/2} \times (E/H)^{2/3} \times (P/c^{3/2}) \quad (3)$$

where P is the indentation load, c is the radial crack length, E is the Young's modulus and H is the hardness. The constants A and n in Eq. (1) have been empirically determined to be 0.016 and 0.5, respectively [28]. In Eq. (2), φ is a material constant and was estimated to be 0.0089 [29]. In Eq. (3), a is the half-diagonal of the indentation impression, l is the crack length from the indentation corner and x_v is a material constant, and was taken to be 0.016 according to previous study [16].

Fracture toughness of the $(Nb,Ti)_3Si$ phase from our experiments was calculated to be 0.8 ± 0.2, 1.0 ± 0.3, and 2.3 ± 1.3 MPa-$m^{1/2}$ according to Eqs. (1), (2) and (3), respectively. It can be seen that applications of those expressions lead to different fracture toughness values. The expression proposed by Laugier yields the highest value, which is almost 2.3 times and 2.8 times larger than the values obtained from the Anstis's expression and Niihara's expression, respectively. The applicability of these three expressions was assessed by Daniel *et al.* [16] in the study of fracture toughness of carbides in steels using nanoindentation. After a careful experimental assessment, they suggested that the expression proposed by Laugier gives the best evaluation of K_c by nanoindnetation at small applied loads, where the cracks are

shorter than 10 μm. In our cases, the longest crack was measured to be ~ 8 μm when the maximum depth of indentation was 1000 nm. Therefore, the fracture toughness value of $(Nb,Ti)_3Si$ in this alloy can be estimated as 2.3 ± 1.3 MPa-$m^{1/2}$. This seems reasonable as the fracture toughness of the monolithic silicide phase Nb_5Si_3 has been reported to be between 1-3 MPa-$m^{1/2}$ [31]. Generally, the fracture toughness values of the $(Nb,Ti)_3Si$ evaluated by Eq.(1)-(3) are very close to that of the monolithic silicide phase Nb_5Si_3.

3.3 Compressive deformation behavior from micropillar compression

In this section, we look at the compressive deformation behavior of both Nbss and the counterpart silicide, $(Nb,Ti)_3Si$. In other words, we are attempting to measure the overall representative mechanical properties of each individual phase in the bulk alloy. In order to do so, it is essential to make sure that the size of the pillar samples is large enough to minimize the effect of sample size on the mechanical behavior, as reported in prior studies [17, 32]. This is also important due to the fact that the damage thickness of gallium (tens of nanometers) caused by ion beam milling can contribute to the mechanical change when the sample size is down to a few hundred nanometers [33]. However, this effect can be reduced significantly when the size of the sample is increased to the microscale.

Figs. 4a and 4b show the typical SEM images of the fabricated micropillars on Nbss and $(Nb,Ti)_3Si$ phases, respectively. The images were taken at an angle of 52^o between the electron beam and the sample axis. It can be seen that the bottom of the

pillars is not visible in some images taken at this angle. Thus, images were also taken at 38^{o}, where the bottom of the pillar was visible, to enable accurate measurement of the initial pillar length and, thus, accurate strain.

Figs. 4c and 4d show the typical deformed micropillars after compression. The compressive stress-strain curves of Nbss and $(Nb,Ti)_3Si$ phases are shown in Fig. 5. The diameter at half height of the pillar was used to calculate stress value. In the case of Nbss, pillars exhibited large plastic deformation during compression, as indicated in the continuous stress-strain curves of Fig. 5a. Small strain bursts/flat platforms observed in some portions of the stress-strain curves are possibly due to the formation of fine slip bands and have been shown to be related to the avalanche-like dislocation events [34]. The same type of stress-strain curves was also observed in the compression of pure Nb micropillars [21-23]. The observed compliance during the initial loading section in the stress-strain curves can be attributed to slight misalignment between the micropillar surface and the flat punch and microscopic roughness of the top of the pillars [35, 36]. Strain hardening is evident in the stress-strain curves of Nbss micropillars. Strain hardening in micropillar compression has been a debatable topic and many variables contribute towards this behavior. It has been proposed that geometry of the pillars, such as taper, can actually introduce artificial strain hardening [37, 38]. The best way to remove the taper of the pillar is to use lathe milling technique developed by Uchic *et al*. [17]. The lathing process was not used in this study due to following two reasons: a) There are some practical difficulties associated with it, and b) it was shown recently by Hutsch *et al*. [39] that

lathe milling leads to overestimation of stress values by about 4 times than the pillars fabricated by annular milling. This was attributed to the very high dose of the ion beam on the surface in the case of lathe milling. Friction between the indenter tip and the top surface of the micropillar can also play an important role in the deformation behavior during compression. In macroscopic compression testing, generally lubrication is applied to remove friction between the platen and the sample surface. There is no way to provide lubrication between flat punch and the pillar top in micropillar compression in nanoindenter. Zhang *et al*. [37] showed that the flow stress can increase due to the presence of friction and the effect increases with increase in aspect ratio. They showed that there is no effect of friction on flow stress when aspect ratio is low (such as 2). However, in the case of aspect ratio of ~3 (which is our case), the effect of friction in increasing flow stress would only be significant after about 9-10% strain which is higher than the values in this study. Raabe *et al*. [40] also found that effect of friction on flow stress is only significant at higher strain values. Moreover, friction has been shown to be helpful in preventing buckling of the micropillar [37, 40, 41]. Therefore, we believe that there should not be a significant effect of friction on flow stress values of Nbss measured here.

The compressed Nbss micropillars exhibited fine and coarse slip bands at the surface, as indicated by arrows in Fig. 4(c). One may also notice that all the slip bands of the Nbss pillars are on single crystallographic planes, which is similar to the observations made in previous compression studies on pure single crystal Nb pillars [21-23]. It has been shown that secondary slip systems were not activated for those

pillars that were compressed to only ~12 % strain, while slip traces were observed along a secondary (less favorable) system in the cases when the strain was higher than ~20% [22]. It seems that the relatively small compressive strain (~12%) in this study was less likely to trigger slip in multiple slip systems.

The yield strength of the Nbss pillars was extracted from the compressive stress-strain curves. The yield stress determined by the 0.2% offset method is 0.9 ± 0.1 GPa. For comparison, the stress at an axial strain of 2.5% was also evaluated, similar to analogous pillar studies [36, 42], and the stress was measured to be 1.0 ± 0.1 GPa. This value is much higher than the reported value of ~350-400 MPa at 2.5% strain for 1-2 μm pure single crystal Nb pillars [22].

The higher yield strength obtained in this study is likely to be caused by solid solution strengthening due to addition of Ti and Si. The stress-strain curves for the $(Nb,Ti)_3Si$ phase are linear until catastrophic failure of the pillars at ~4-5% strain (Fig. 5b). The absence of plastic deformation indicates that the silicides $(Nb,Ti)_3Si$ are quite brittle in nature. The compressed pillar of $(Nb,Ti)_3Si$ (Fig. 4d) shows a typical brittle fracture by cleavage along certain planes, as shown by arrows. The morphology of some compressed pillars illustrate that $(Nb,Ti)_3Si$ pillars were fractured by cleavage along certain planes. A similar fracture mode was also previously detected in the microcompression of Al_7Cu_2Fe inclusions in Al 7075 whose mechanical properties were also reported to be brittle in nature [15].

Fig. 5c shows the stress-strain curves of both Nbss and $(Nb,Ti)_3Si$ pillars for comparison. It is evident that the strength of $(Nb,Ti)_3Si$ pillars is much higher than

that of the Nbss. The compressive failure strength of $(Nb,Ti)_3Si$, was measured to be 8.4 ± 1.2 GPa. Failure strength in the case of $(Nb,Ti)_3Si$ is defined as the stress value where the large strain burst occurred. Higher hardness is reported to relate to higher yield strength and tensile strength in the materials [43]. Qualitatively, the stress values here agree with the hardness results obtained by nanoindentation. The mechanical properties of individual phase are very useful in understanding the mechanical behavior of the bulk material. For example, the existence of the harder and stronger $(Nb,Ti)_3Si$ phase contributes to the high strength of the Nb-based alloys, while the ductile phase, Nbss, in the alloy bears a larger degree of plastic deformation under the applied load. A similar correlation has also been found in other plastic materials, such as dual phase steels, where the strong martensitic phase was found to bear higher stress than the ferritic phase [44-47].

In order to evaluate accurate deformation behavior of the constituent phases, it was necessary to make sure that the micropillar was of the same phase along the sample height. Usually, this can be confirmed by either EDS compositional analysis after the fabrication of the micropillar or by observation of the shape of the stress-strain curves. However, due to the relatively small phase size, pillars containing another phase at the base are possible and inevitable for some cases. Fig. 6(a-d) show some selected SEM images of the deformed $(Nb,Ti)_3Si$ micropillars with Nbss at the base along with the stress-strain curves. In this study, the phases along the pillar height were determined by EDS analysis. It is seen that pillars with Nbss at the base mainly deformed by slipping at the phase boundary or in the Nbss phase itself, as

indicated by arrows in Fig. 6(a-c). It is pointed out that the different deformation behavior of the pillars for the $(Nb,Ti)_3Si$ phase with Nbss base might be due to the geometrical difference of grain boundary or phase boundary. However, the examination of the geometry of the phase boundary for the pillar is almost impossible and thus, cannot be directly related to the deformation behavior. We also would like to point out that the detailed study of the deformation of pillar due to the geometrical difference of phase boundary is not the focus of the current study. Very complex stress-strain curves of these pillars were observed as opposed to the brittle failure of pillars with pure $(Nb,Ti)_3Si$ phase. Due to the presence of the softer Nbss at the base, the stress required for the same strain value decreased dramatically compared to the pillars of pure $(Nb,Ti)_3Si$ phase, although it's still much higher than that of the pure Nbss micropillars, i.e, ~1.5 GPa for pillar in Fig. 6a compared to that of ~1 GPa in the pure Nbss pillars at the same strain of ~2.5%. With combined observations of the post deformation and the stress-strain curve of each micropillar, the results of the micropillars containing Nbss at the base were removed from further analysis.

It should be mentioned here that the so called "size effect" phenomenon [17], may also exist in the pillars in this study. To study this, we also attempted to fabricate larger pillars; however, due to very small size of phases most of them exhibited Nbss at the base. Even in 1.7-1.9 μm diameter pillars fabricated in this study, the base of several pillars was of Nbss, as mentioned above. Thus, we believe the size of micropillar size, and thus, its mechanical properties, are consistent with what would be observed for the size of the particles observed in the microstructure of this alloy.

The results obtained in this study should contribute to an understanding of the mechanical behavior of the bulk materials, and can be used for modeling purposes as constituent behavior of the phases.

4. Summary

Nanoindentation and micropillar compression techniques were used to investigate the micromechanical behavior of Nbss and $(Nb,Ti)_3Si$ phases in a Nb-16Si-22Ti alloy. Qualitatively, mechanical tests indicated brittle behavior of the $(Nb,Ti)_3Si$ phase, while the Nbss exhibited a much higher degree of plasticity. Moreover, $(Nb,Ti)_3Si$ was shown to possess much higher hardness, Young's modulus and compressive stress than the Nbss counterpart.

Fracture toughness of $(Nb,Ti)_3Si$ phase was evaluated to be ~2.3 MPa-$m^{1/2}$ using Laugier's expression by nanoindentation. The microcompression results of 1.7-1.9 μm pillars suggested that Nbss had a yield stress of 0.9 ±0.1 GPa, while for $(Nb,Ti)_3Si$ phase, a failure strength of 8.4 ± 1.2 GPa had been detected. The quantified critical properties of constituents obtained in this study will allow better understanding of the bulk material deformation of this Nb-Si-Ti based alloy and can be further incorporated into mechanical models for simulation studies.

Acknowledgements

This work was financially supported by the National Science Foundation of China (Grant No. 51404016 and No. 51405458). MYW acknowledges the

Postdoctoral Science Foundation of China (Grant No. 2014M550588). We acknowledge the use of the focus ion beam at the Leroy Eyring Center for Solid State Science (LE-CSSS) at Arizona State University. We also thank Carl Mayer at the Arizona State University for helpful discussions.

References

[1] B. P. Bewlay, M. R. Jackson and H. A. Lipsitt, Metallurgical and Materials Transactions a-Physical Metallurgy and Materials Science, 27 (1996) 3801-3808.
[2] B. P. Bewlay, M. R. Jackson, J. C. Zhao and P. R. Subramanian, Metallurgical and Materials Transactions a-Physical Metallurgy and Materials Science, 34A (2003) 2043-2052.
[3] B. P. Bewlay, M. R. Jackson, J. C. Zhao, P. R. Subramanian, M. G. Mendiratta and J. J. Lewandowski, Mrs Bulletin, 28 (2003) 646-653.
[4] Z. Li and L. M. Peng, Acta Materialia, 55 (2007) 6573-6585.
[5] Y. Yan, H. Ding, Y. Kang and J. Song, Materials & Design, 55 (2014) 450-455.
[6] N. Sekido, Y. Kimura, S. Miura, F.-G. Wei and Y. Mishima, Journal of Alloys and Compounds, 425 (2006) 223-229.
[7] J. L. Yu and K. F. Zhang, Scripta Materialia, 59 (2008) 714-717.
[8] W. Y. Kim, I. D. Yeo, T. Y. Ra, G. S. Cho and M. S. Kim, Journal of Alloys and Compounds, 364 (2004) 186-192.
[9] S. Kashyap, C. S. Tiwary and K. Chattopadhyay, Intermetallics, 19 (2011) 1943-1952.
[10] J. R. Zhou and J. B. Sha, Intermetallics, 34 (2013) 1-9.
[11] K. S. Chan, Materials Science and Engineering a-Structural Materials Properties Microstructure and Processing, 329 (2002) 513-522.
[12] M. R. Jackson, B. P. Bewlay, R. G. Rowe, D. W. Skelly and H. A. Lipsitt, Jom-Journal of the Minerals Metals & Materials Society, 48 (1996) 39-44.
[13] B.P. Bewlay, M.R. Jackson, H.A. Lipsitt, MRS Symp. Proc., 460 (1997) 715.
[14] S. Qu, Y. Han and L. Song, Intermetallics, 15 (2007) 810-813.
[15] S. S. Singh, E. Guo, H. Xie and N. Chawla, Intermetallics, 62 (2015) 69-75.
[16] D. Casellas, J. Caro, S. Molas, J. M. Prado and I. Valls, Acta Materialia, 55 (2007) 4277-4286.
[17] M. D. Uchic, D. M. Dimiduk, J. N. Florando and W. D. Nix, Science, 305 (2004) 986-989.
[18] J. R. Greer and W. D. Nix, Applied Physics a-Materials Science & Processing, 80 (2005) 1625-1629.
[19] Z. W. Shan, R. K. Mishra, S. A. S. Asif, O. L. Warren and A. M. Minor, Nature Materials, 7 (2008) 115-119.

[20] E.-Y. Guo, H.-X. Xie, S. S. Singh, A. Kirubanandham, T. Jing and N. Chawla, Materials Science and Engineering a-Structural Materials Properties Microstructure and Processing, 598 (2014) 98-105.
[21] K. J. Hemker and W. N. Sharpe, Jr., Annual Review of Materials Research, 37 (2007) 93-126.
[22] A. S. Schneider, D. Kaufmann, B. G. Clark, C. P. Frick, P. A. Gruber, R. Moenig, O. Kraft and E. Arzt, Physical Review Letters, 103 (2009)
[23] A. S. Schneider, C. P. Frick, B. G. Clark, P. A. Gruber and E. Arzt, Materials Science and Engineering a-Structural Materials Properties Microstructure and Processing, 528 (2011) 1540-1547.
[24] H. Fei, A. Abraham, N. Chawla and H. Jiang, Journal of Applied Mechanics-Transactions of the Asme, 79 (2012)
[25] N. Sekido, Y. Kimura, S. Miura and Y. Mishima, Materials Science and Engineering a-Structural Materials Properties Microstructure and Processing, 444 (2007) 51-57.
[26] Y. X. Tian, J. T. Guo, L. Y. Sheng, G. M. Cheng, L. Z. Zhou, L. L. He and H. Q. Ye, Intermetallics, 16 (2008) 807-812.
[27] Y. X. Tian, J. T. Guo, G. M. Cheng, L. Y. Sheng, L. Z. Zhou, L. L. He and H. Q. Ye, Materials & Design, 30 (2009) 2274-2277.
[28] G. R. Anstis, P. Chantikul, B. R. Lawn and D. B. Marshall, Journal of the American Ceramic Society, 64 (1981) 533-538.
[29] K. Niihara, Journal of Materials Science Letters, 2 (1983) 221-223.
[30] M. T. Laugier, Journal of Materials Science Letters, 6 (1987) 897-900.
[31] P.R. Subramanian, M.G. Mendiratta, D.M. Dimiduk, MRS Symp. Proc., 322(1994) 491-502.
[32] J. R. Greer, W. C. Oliver and W. D. Nix, Acta Materialia, 53 (2005) 1821-1830.
[33] D. Kiener, C. Motz, M. Rester, M. Jenko and G. Dehm, Materials Science and Engineering a-Structural Materials Properties Microstructure and Processing, 459 (2007) 262-272.
[34] D. M. Dimiduk, C. Woodward, R. LeSar and M. D. Uchic, Science, 312 (2006) 1188-1190.
[35] R. Soler, J. M. Molina-Aldareguia, J. Segurado, J. Llorca, R. I. Merino and V. M. Orera, International Journal of Plasticity, 36 (2012) 50-63.
[36] C. P. Frick, B. G. Clark, S. Orso, A. S. Schneider and E. Arzt, Materials Science and Engineering a-Structural Materials Properties Microstructure and Processing, 489 (2008) 319-329.
[37] H. Zhang, B. E. Schuster, Q. Wei and K. T. Ramesh, Scripta Materialia, 54 (2006) 181-186.
[38] D. Kiener, C. Motz and G. Dehm, Materials Science and Engineering a-Structural Materials Properties Microstructure and Processing, 505 (2009) 79-87.
[39] J. Huetsch and E. T. Lilleodden, Scripta Materialia, 77 (2014) 49-51.
[40] D. Raabe, D. Ma and F. Roters, Acta Materialia, 55 (2007) 4567-4583.

[41] M. D. Uchic, P. A. Shade, D. M. Dimiduk, Annu. Rev. Mater. Res. 39 (2009) 361-386.
[42] J. R. Greer and W. D. Nix, Physical Review B, 73 (2006)
[43] P. Zhang, S. X. Li and Z. F. Zhang, Materials Science and Engineering a-Structural Materials Properties Microstructure and Processing, 529 (2011) 62-73.
[44] J. L. Stewart, L. Jiang, J. J. Williams and N. Chawla, Materials Science and Engineering a-Structural Materials Properties Microstructure and Processing, 534 (2012) 220-227.
[45] J. L. Stewart, J. J. Williams and N. Chawla, Metallurgical and Materials Transactions a-Physical Metallurgy and Materials Science, 43A (2012) 124-135.
[46] J. J. Williams, J. L. Walters, M. Y. Wang, N. Chawla and A. Rohatgi, Jom, 65 (2013) 226-233.
[47] H. Ghassemi-Armaki, R. Maass, S. P. Bhat, S. Sriram, J. R. Greer and K. S. Kumar, Acta Materialia, 62 (2014) 197-211.

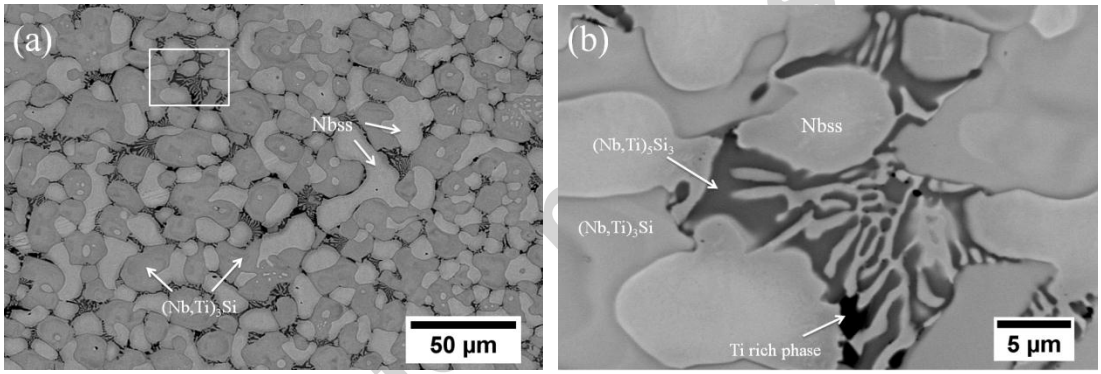

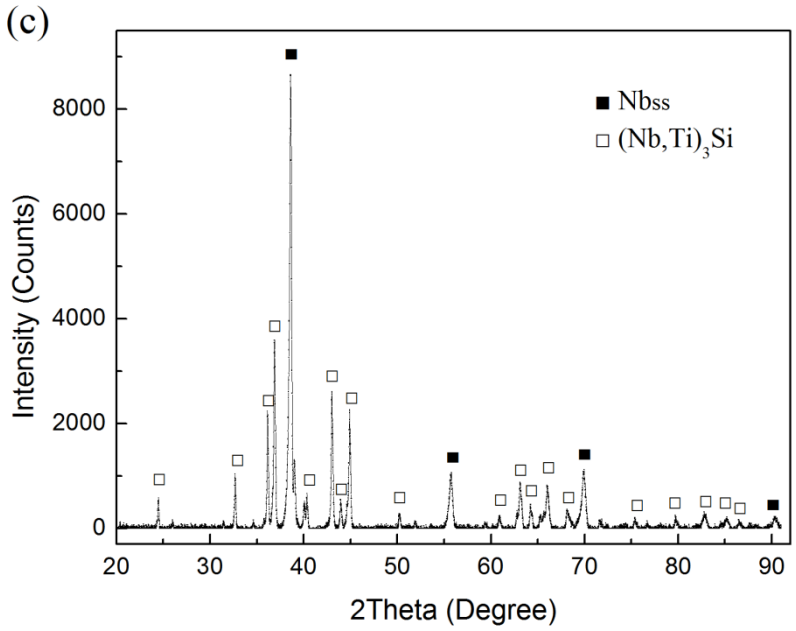

Figure 1. (a) Back-scattered electron image showing the Nb solid solution (Nbss) and intermetallic phase ($(Nb,Ti)_3Si$, $(Nb,Ti)_5Si_3$,) in the Nb-16at.%Si-22at.%Ti alloy (b) magnified back-scattered electron image of region, as indicated by rectangle in (a); The dark phase in (b) is identified as a combination of Nb_5Si_3 and Ti rich phases by EDS. (c) X-ray diffraction patterns of the as-cast sample.

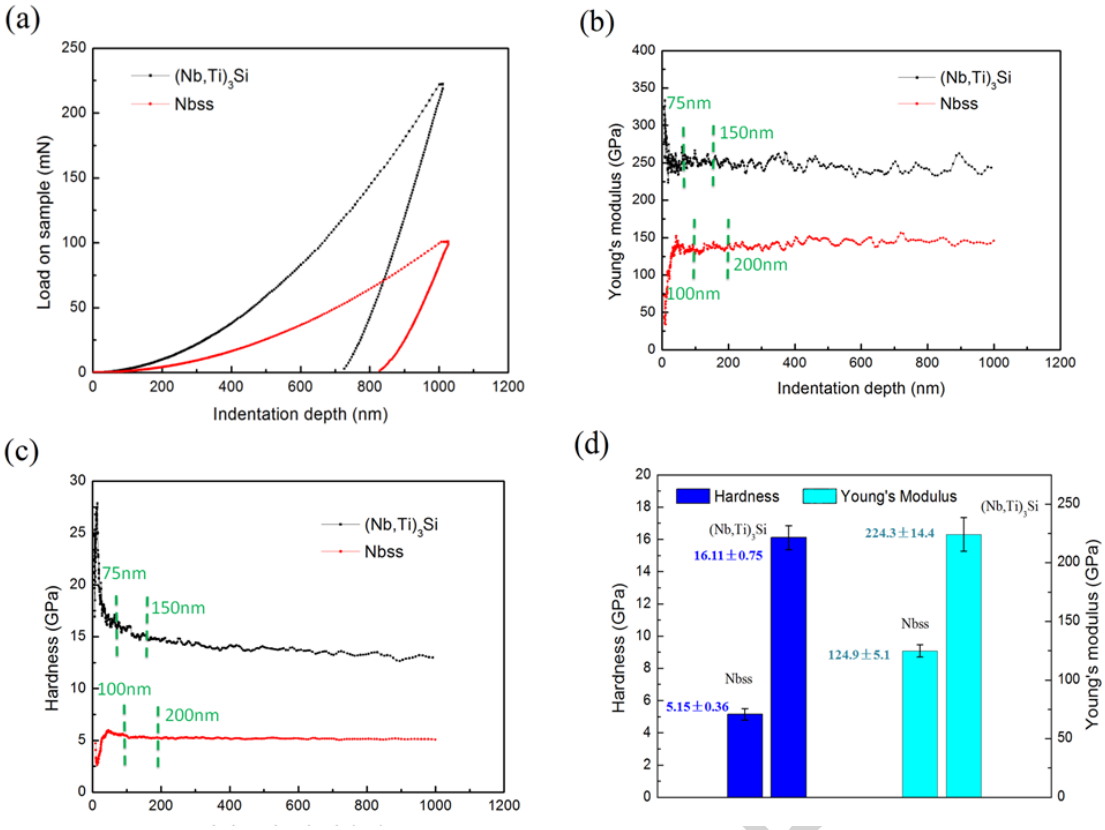

Figure 2. Typical results of nanoindentation on Nbss and $(Nb,Ti)_3Si$ in the Nb-16at.%Si-22at.%Ti alloy: (a) load on sample; (b) Young's modulus versus indentation depth; (c) hardness versus indentation depth; (d) summarized average hardness and Young's modulus values.

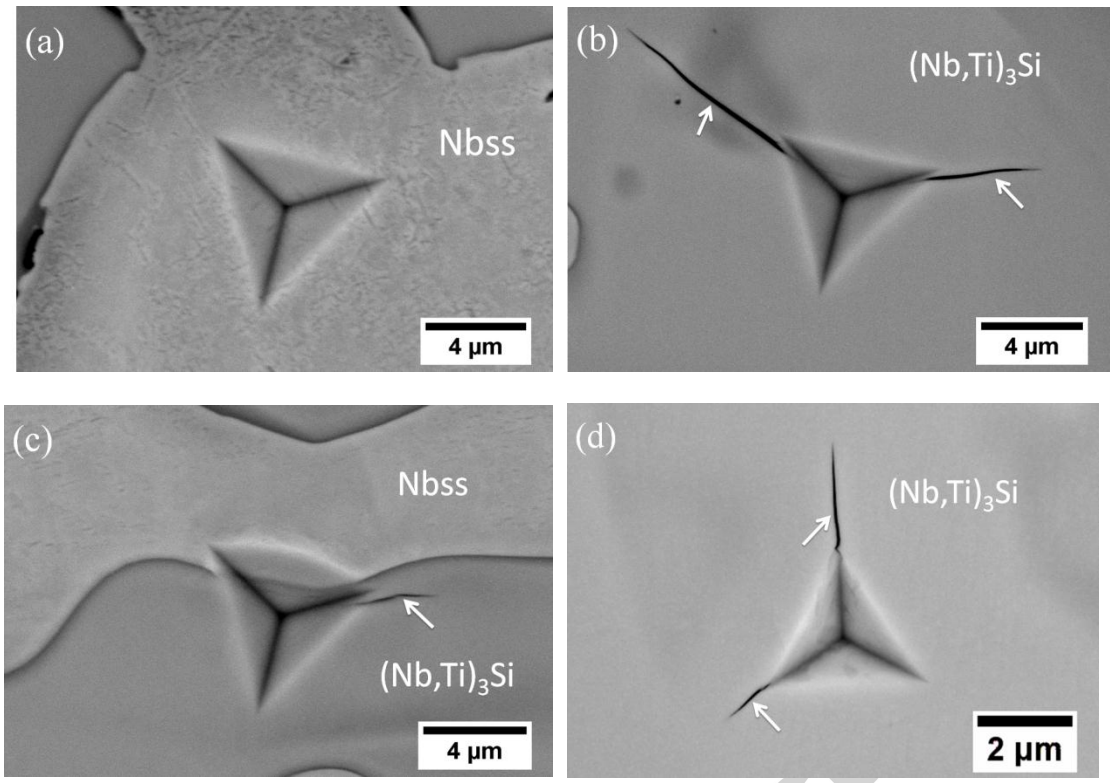

Figure 3. BSE images showing the deformation around the indentations for: (a) Nbss, (b), (d) $(Nb,Ti)_3Si$, and (c) combined Nbss and $(Nb,Ti)_3Si$ phases. White arrows in (b), (c) and (d) show indentation cracks in the $(Nb,Ti)_3Si$ phase. Indentation depth for (a), (b), and (c) is 1000 nm, while 500 nm for (d).

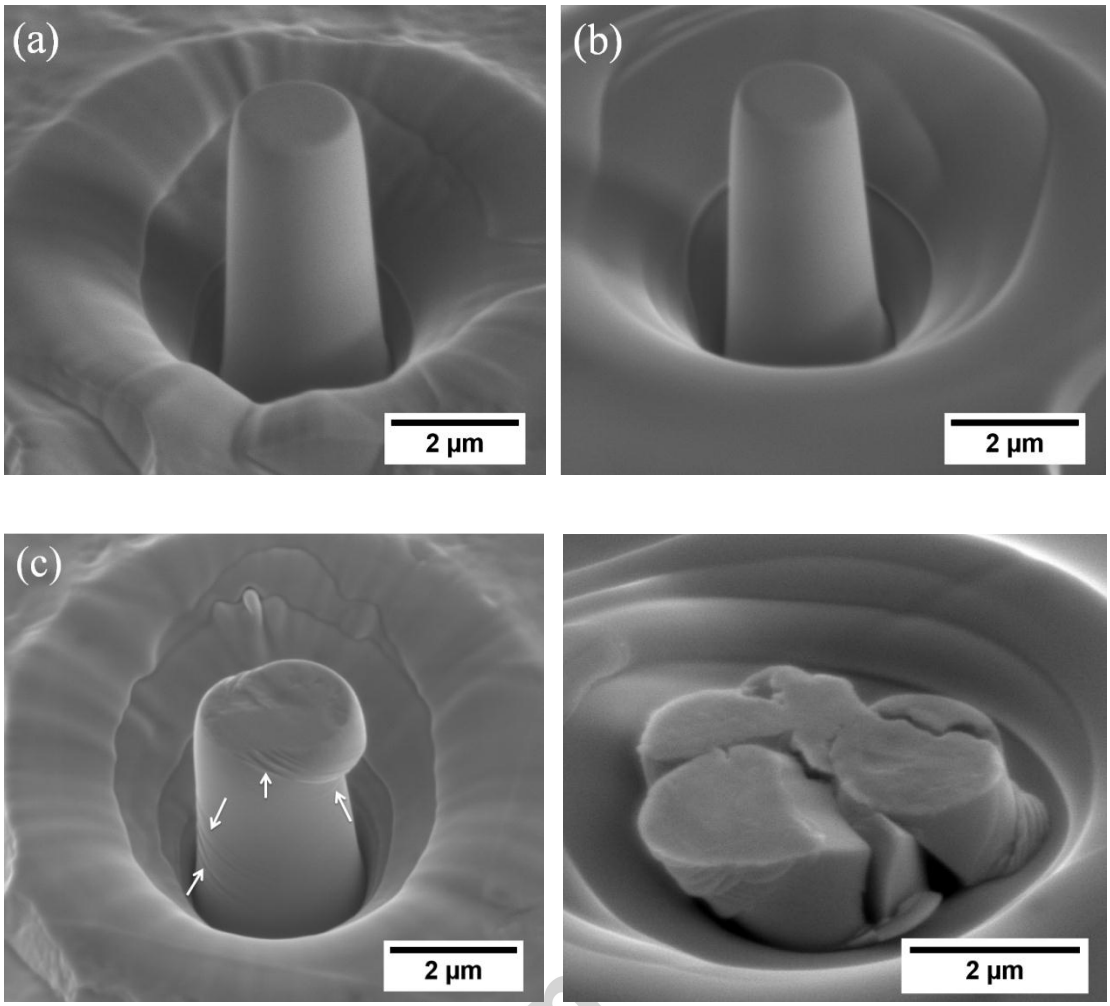

Figure 4. Representative SEM images of micropillars fabricated using FIB before deformation: (a) Nbss, (b) $(Nb,Ti)_3Si$; and after deformation: (c) Nbss, (d) $(Nb,Ti)_3Si$. Samples were tilted 52^o for (a), (b), (d) and 35^o for (c) when the images were taken.

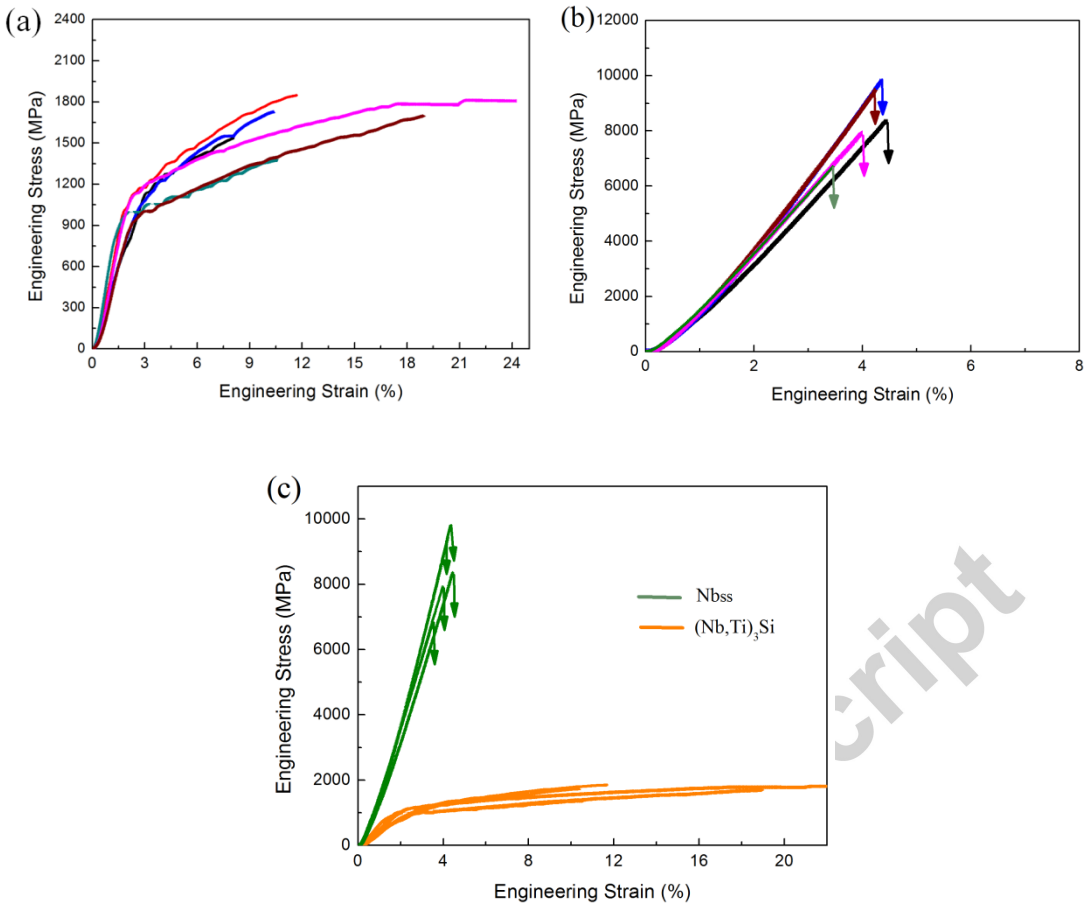

Figure 5. Compressive stress-strain curves of the micropillars for (a) Nbss, (b) $(Nb,Ti)_3Si$, (c) combination of Nbss and $(Nb,Ti)_3Si$

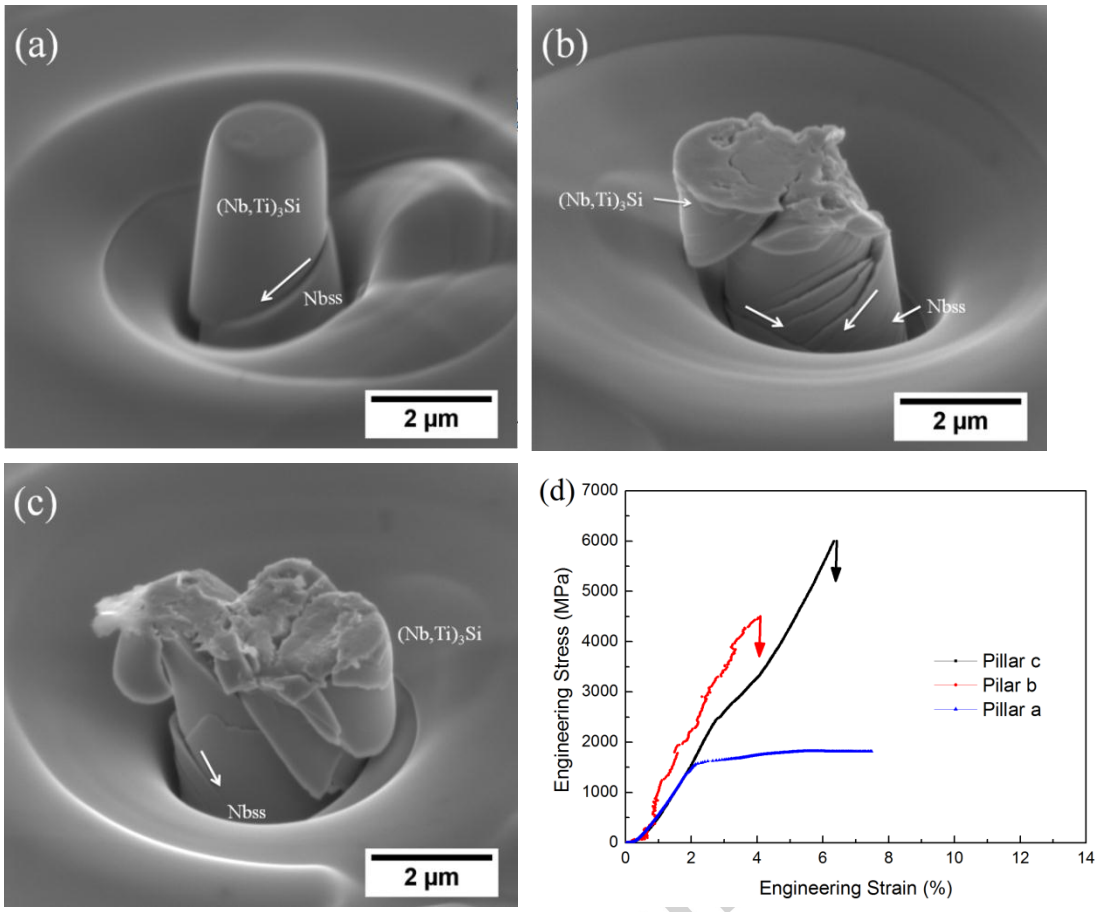

Figure 6. Deformation of $(Nb,Ti)_3Si$ phase with Nbss at the base: (a), (b) and (c) SEM images showing different deformation behavior of the micropillars (d) stress-strain curves of the pillars due to the presence of Nbss at the base.

Table 1 EDS analysis of phases in Nb-16Si-22Ti alloy (in at.%)

	Nb	Ti	Si
Nbss	74.5 ± 0.2	22.5 ± 0.4	3.0 ± 0.3
$(Nb,Ti)_3Si$	58.6 ± 2.9	17.2 ± 3.2	24.2 ± 0.3
$(Nb,Ti)_5Si_3$	33.8 ± 0.4	30.4 ± 0.2	35.8 ± 0.3